An Accreting Supermassive Black Hole Buried in a Faint Dwarf Galaxy

Abhishek Paswan[1,2] , Mousumi Das[1] , and K Rubinur[3,4]

[1] Indian Institute of Astrophysics, Koramangala II Block, Bangalore 560034, India; apaswan@allduniv.ac.in
[2] Department of Physics, University of Allahabad, Prayagraj 211002, India
[3] Institute of Theoretical Astrophysics, University of Oslo, P.O. Box 1029, Blindern, 0315 Oslo, Norway
[4] National Centre for Radio Astrophysics—Tata Institute of Fundamental Research, Ganeshkhind, Pune 411007, India

Abstract

In the last decade, there have been several discoveries of active galactic nuclei (AGN) in dwarf galaxies including an AGN in an ultracompact dwarf galaxy with a black hole mass $>10^6\,M_\odot$. However, finding a supermassive black hole (SMBH) in a dwarf low surface brightness (LSB) galaxy is rare. We report the discovery of a Seyfert type 2 class AGN that is associated with a nuclear SMBH of mass $\sim 6.5 \times 10^6\,M_\odot$ in a dwarf LSB galaxy ($\mu_{0,r} > 23.8$ mag arcsec^{-2}) that we denote by MJ0818+2257. The galaxy was previously thought to be an outlying emission blob around the large spiral galaxy LEDA 1678924. In our current analysis, which includes the detection of the optical counterpart of MJ0818+2257, we study its ionized gas kinematics and find that the dynamical mass within the ionized gas disk is $\sim 5.3 \times 10^9\,M_\odot$. This is comparable to its stellar mass, which is $\sim 3 \times 10^9\,M_\odot$, and suggests that MJ0818+2257 is moderately dark matter dominated within the stellar disk. The SMBH-mass-to-galaxy-stellar-mass ratio is $M_{\rm BH}/M^{(*)} > 0.022$, which is high compared to disk galaxies. Our detection of an SMBH in a bulgeless LSB dwarf galaxy raises questions about the growth of SMBHs in low-luminosity galaxies and suggests the possibility of detecting heavy seed black holes from early epochs in LSB dwarf galaxies in the low-redshift Universe.

Unified Astronomy Thesaurus concepts: Active galactic nuclei (16); AGN host galaxies (2017); Dwarf galaxies (416); Low surface brightness galaxies (940)

1. Introduction

One of the fundamental open problems of current observational cosmology is to understand the formation of the first black holes (BHs; J. Bellovary et al. 2011). It is not clear how the initial seed BHs formed in the early Universe, what their properties were, and what the nature of their host galaxies was. In the literature, supermassive BH (SMBH) masses strongly correlate with many properties of the host galaxies and bulges across cosmic time, which only implies coevolution (e.g., K. Gebhardt et al. 2000; L. Ferrarese & D. Merritt 2000; A. Marconi & L. K. Hunt 2003; N. J. McConnell & C.-P. Ma 2013). However, unlike massive galaxies, low-luminosity dwarfs do not have bulges, nor do they appear to have undergone a rich merger history. Hence, finding active galactic nuclei (AGN) in these galaxies is surprising. Also, since their merger history is poor, the BHs associated with their AGN may be similar to the first seed BHs (J. Bellovary et al. 2011). Direct observational detection of seed BHs in massive galaxies is difficult with current capabilities as they are at very high redshifts. The discovery of more and more very massive SMBH at very high redshifts requires either super-Eddington accretion, very large seed BHs, or both; the nearby faint dwarf galaxies are within our observational reach and can put important constraints on the connection between the host galaxies and their seed BHs (M. Volonteri 2010; J. E. Greene 2012).

A few studies, including NGC 4395, confirm the detection of AGN having intermediate-mass BHs (IMBHs) and SMBHs in low-mass dwarf galaxies (e.g., A. E. Reines et al. 2011; A. E. Reines & A. T. Deller 2012; A. E. Reines et al. 2016, 2020). However, the detection of an AGN associated with an SMBH in a bulgeless, low surface brightness (LSB) dwarf galaxy is rare and cannot be explained by conventional galaxy evolution theories or the $M_{\rm BH}$–σ_* relation (N. J. McConnell & C.-P. Ma 2013). Such a detection, however, may provide better constraints to the limiting mass of seed BHs and their growth in early epochs. This is especially important since the James Webb Space Telescope (JWST) has detected surprisingly massive BHs in small galaxies (F. Pacucci et al. 2023).

Here we present the serendipitous discovery of a bulgeless, LSB dwarf galaxy hosting an AGN observed with the integral field unit (IFU) spectroscopy (N. Drory et al. 2015) in the Mapping Nearby Galaxies at Apache Point Observatory (MaNGA; K. Bundy et al. 2015) survey. This galaxy, which we name as MJ0818+2257, was earlier thought to be an emission blob (O. Bait et al. 2019) lying outside the large spiral galaxy, LEDA 1678924, and its close lenticular companion galaxy, LEDA 1678982 (see Figures 1(a)–(d)). This outlying emission blob was thought to be a Hanny's Voorwerp (HsV) object illuminated by the AGN activity of LEDA 1678924 (O. Bait et al. 2019). However, our investigation shows that there is an optical counterpart to the emission blob, and it is also associated with a rotating disk of ionized gas. Hence, the emission blob is actually a bulgeless LSB dwarf galaxy, MJ0818+2257, and the ionized gas is due to AGN activity in the galaxy.

Throughout the Letter, we have considered a flat ΛCDM cosmology with $H_0 = 70$ km s^{-1} Mpc^{-1}, $\Omega_m = 0.3$, and $\Omega_\Lambda = 0.7$, where H_0 represents the Hubble constant and Ω_m and Ω_Λ are matter and dark energy density, respectively. All the
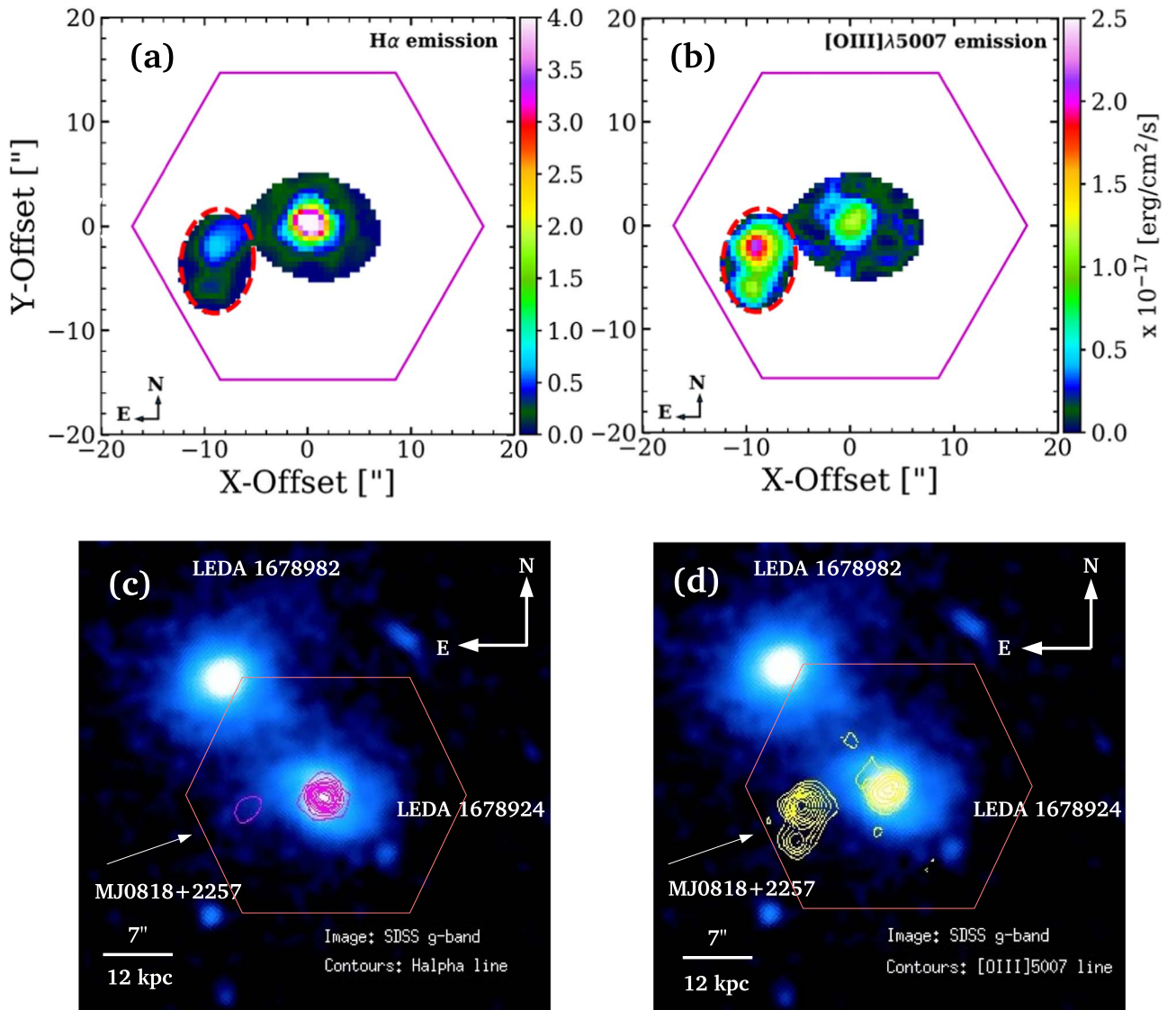
Figure 1. Panels (a) and (b) show the Hα and [O III]λ5007 emission-line maps, respectively. In the emission-line maps, the outlying emission blob (which we later name as MJ0818+2257) is marked with a red dashed ellipse. Panels (c) and (d) represent the SDSS *g*-band image overlaid with the Hα (red) and [O III]λ5007 (yellow) emission-line contours, indicating that there is no optical counterpart of the outlying emission blob.

magnitudes quoted in this Letter are in the AB system (J. B. Oke 1974).

2. Data and Analysis

2.1. Optical Imaging and IFU Data

This study uses publicly available optical images from the Sloan Digital Sky Survey (SDSS) DR17, which reaches 5σ magnitudes of 23.13, 22.7, and 20.71 mag in the *g*, *r*, and *z* bands, respectively. We also use optical images from the Dark Energy Camera Legacy Survey (DECaLS) DR9, reaching 5σ depths of 24.0, 23.4, and 22.5 mag in the *g*, *r*, and *z* bands, respectively. The DECaLS images have been mainly used for detecting the optical counterparts of the target source.

The optical IFU data used in the present work comes from the MaNGA survey. We use data cubes that have been reduced and calibrated using the Data Reduction Pipeline (DRP; D. R. Law et al. 2016). In the final data cubes, the calibrated spectra have a wavelength coverage of 3600–10300 Å with a spectral resolution of $R \sim 2000$. These calibrated data cubes are

then made into science-ready products using Data Analysis Pipeline (DAP; K. B. Westfall et al. 2019). This work uses the DAP output products. The DAP uses pPXF code (M. Cappellari & E. Emsellem 2004), which fits the models to both the stellar continuum and emission-line features, e.g., emission and absorption lines, identified in the spectra from each spaxel. Various gas emission–line fluxes are derived from Gaussian model fits after subtracting the stellar continuum and absorption lines and then provided in the form of 2D maps. The Galactic reddening correction to the line fluxes is applied assuming the reddening law provided by J. E. O'Donnell (1994). Throughout this work, we have used only spaxels with signal-to-noise ratio $\geqslant 3$.

2.2. Radio Continuum

All the radio images are derived using archival Very Large Array (VLA) data. The 1.4 GHz radio continuum image is taken from the Faint Images of the Radio Sky at Twenty-Centimeters survey. This survey provides radio continuum images of sources
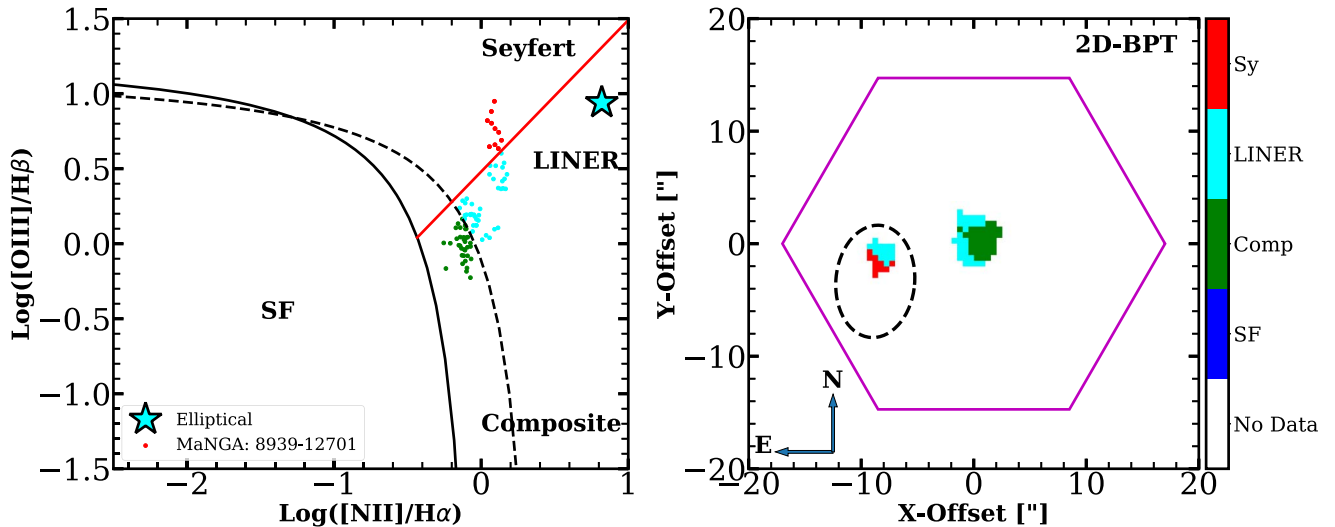
Figure 2. Left: the BPT diagram labeled according to the different regions related to star formation (SF), AGN (Seyfert or LINER), and composite (AGN+SF) activities. Spaxels from LEDA 1678924 and MJ0818+2257 are denoted by dots, while the star symbol represents the data point for LEDA 1678982 (see Figures 1(c) and (d)). Right: the color-coded spatially resolved 2D-BPT diagram corresponds to the left figure.

with a typical rms of 0.15 mJy beam^{-1} and an angular resolution of 5″ (R. H. Becker et al. 1995). Quick Look images from the Karl G. Jansky Very Large Array Sky Survey (VLASS; M. Lacy et al. 2020) are also used for our investigation. The VLASS provides S-band images centered at 3 GHz with an angular resolution of 2″.5. Furthermore, we have analyzed higher-frequency C-, X- and K-band data obtained from VLA archive (ID AG617). The observations were carried out on 2001 September 14–15 in C configuration centered at 4.84 GHz (C band), 8.46 GHz (X band) and 22.5 GHz (K band). Each band has two channels with 50 MHz each, i.e., a total bandwidth of 100 MHz. The target region was observed for 30 s along with the phase calibrator 0854+201 for 90–100 s and flux calibrator 1331 +305 for 30 s. These data are reduced and analyzed using the Common Astronomy Software Applications. We have followed usual data reduction methods, which include flagging of bad data, setting the model for flux calibrator, initial phase calibration, and then gain calibrations of calibrators. Finally, the solutions are applied to the science target. After a satisfactory calibration, the images are obtained using the CLEAN task. As these are snapshot observations with a small exposure time, we are bound to perform only a single round of self-calibration to improve the images.

2.3. Data in Other Bands

Apart from the above-described data sets, we also searched for emissions associated with the target source in the far-ultraviolet (FUV) and X-ray bands using images from the Galaxy Evolution Explorer and Chandra surveys, respectively. We did not detect any emission in either wave band.

3. Results

All the images shown together in Figure 1 clearly indicate the presence of an outlying emission blob marked by the red ellipse in the emission-line maps. Also, its equivalent width (EW; Hα) ranges over 5–15 Å. Since the ionized gas with EW(Hα) < 3 Å is defined as diffuse ionized gas (DIG) in galaxies (e.g., R. Cid Fernandes et al. 2010; K. Zhang et al. 2017; E. A. D. Lacerda et al. 2018), this outlying emission blob rules out the possibility that it is contaminated by DIG.

3.1. Spatially Resolved 2D Baldwin, Phillips, and Terlevich Diagram

We use the Baldwin, Phillips, and Terlevich (BPT; J. A. Baldwin et al. 1981) diagnostic diagram to explore the nature of the outlying emission blob, including LEDA 1678924 and LEDA 1678982. The MaNGA IFU data provide spatially resolved emission-line data for sources in the MaNGA hexagonal footprint as shown in the right panel of Figure 2. In the case of LEDA 1678982, exploring its spatially resolved 2D-BPT diagnostic is impossible due to the unavailability of IFU data. From our derived spatially resolved 2D-BPT diagnostic, we find that composite and LINER-like AGN activities are the primary sources of the ionized gas in the central region of LEDA 1678924. However, in the case of the outlying emission blob, it is due to pure AGN activity composed of LINER and Seyfert-like activity. The nucleus of LEDA 1678982 indicates LINER-like ionization as shown by the star symbol in the left panel of Figure 2, which is derived using a 3″ fiber slit spectrum observed in the SDSS survey.

3.2. Detection of the Optical Counterpart of the Outlying Emission Blob

In Figure 3(a), the DECaLS g-band image available via the recent data release (DR9) clearly shows the detection of an optical counterpart of the outlying emission blob. It is unlikely that this optical detection is due to strong gas line–emission falling in the filter bands because the strongest emission line [O III]λ5007 and other lines around this wavelength fall outside the g band (see Figure 7 in the Appendix). Moreover, a very faint detection is also noticed in the r-, i- and z-band images taken from the DECaLS survey (see Figure 6 in the Appendix). Figure 3(b) shows the continuum- and stellar absorption–subtracted emission-line spectra taken at the center of the outlying emission blob (red) and LEDA 1678924 (spiral galaxy; blue), whose subimages with normalized flux around the rest wavelengths of [O III]λ4958,5007, Hβ and Hα, [N II]λ6548,6583 emission lines are shown in Figures 3(b1) and (b2), respectively. These emission lines indicate that the outlying emission blob and LEDA 1678924 are at different redshifts of 0.09192 ± 0.00001
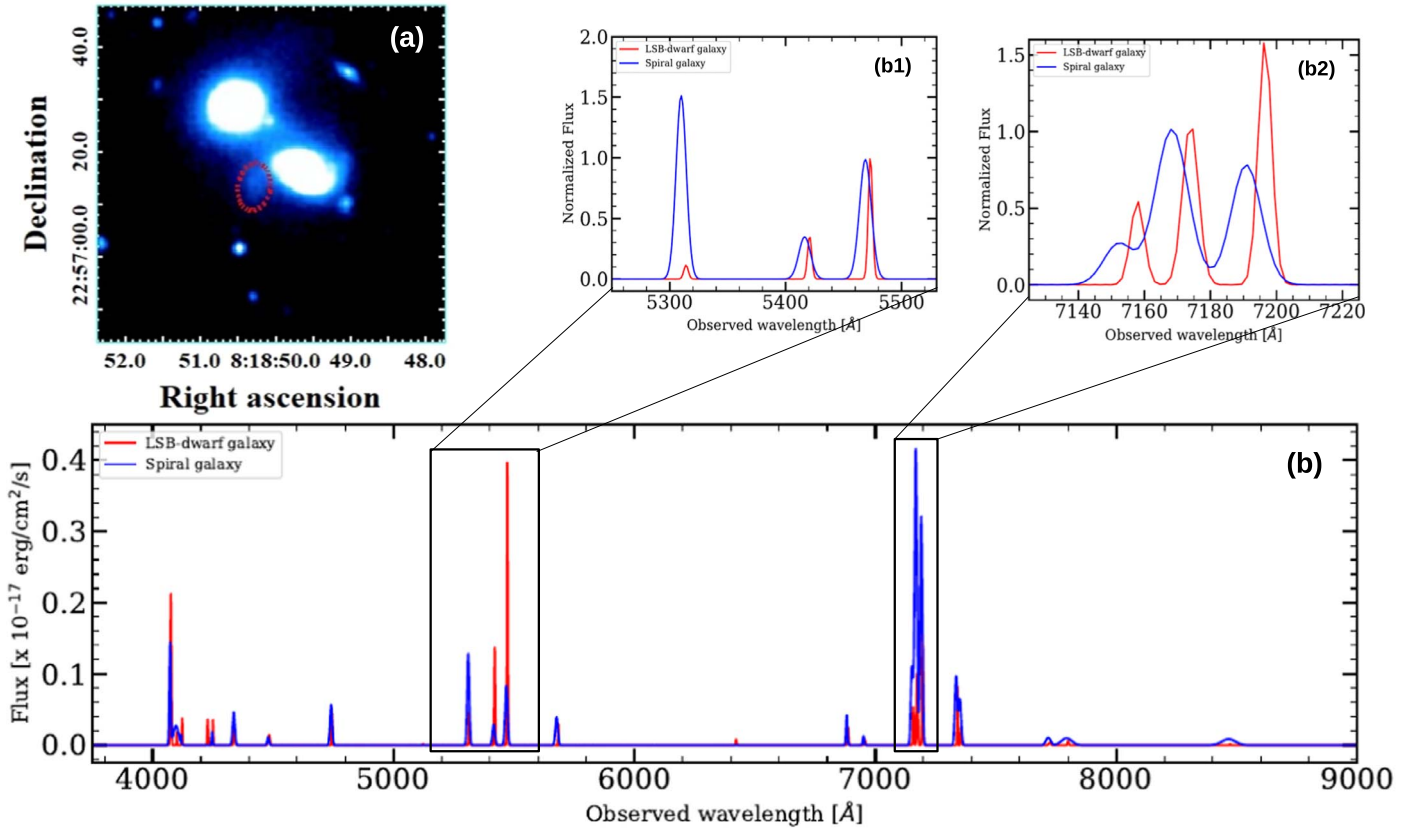
Figure 3. Panel (a) shows the DECaLS g-band image of MaNGA target 1-383997, i.e., LEDA 1678924. The detection of optical counterpart of MJ0818+2257 is marked by red ellipse. Panel (b) represents the stellar continuum– and absorption-subtracted observed spectra of LEDA 1678924 (i.e., spiral galaxy) and outlying emission blob (i.e., LSB dwarf galaxy). Panel (b1) shows the zoomed-in view of Hβ [O III]λ4959,5007 emission lines. Similarly, panel (b2) presents the zoomed-in view of [N II]λ6548,6583 and Hα emission lines.

Table 1
Basic Parameters of the Galaxies, Where Projected Separation is with Respect to MJ0818+2257

Source	R.A. (J2000) (hh:mm:ss)	Decl. (J2000) (dd:mm:ss)	Redshift (z)	Projected Separation (kpc)	Linear Size (kpc)
MJ0818+2257	08:18:50.238	+22:57:14.86	0.09294 ± 0.00012	0	16.9
LEDA 1678924	08:18:49.617	+22:57:16.39	0.09192 ± 0.00001	16.9	34.9
LEDA 1678982	08:18:50.523	+22:57:29.03	0.09239 ± 0.00013	26.0	40.2

and 0.09294 ± 0.00012, respectively (see Table. 1). The third system in the field, LEDA 1678982, is at a redshift of 0.09239 ± 0.00013, derived using a 3″ fiber slit spectrum observed in the SDSS survey. This implies that all the three systems, within the errors, are at different redshifts, and the outlying emission blob is the most redshifted relative to LEDA 1678924 and LEDA 1678982. In Table 1, it can be seen that LEDA 1678924 and LEDA 1678982 are separated by projected distances of ∼16.9 and ∼26 kpc, respectively, from the outlying emission blob. These results reveal the possibility of the existence of a very faint, low-mass dwarf galaxy candidate (hereafter named as MJ0818+2257) contributing to the stellar emission at the location of the outlying emission blob.

3.3. Kinematics of the Emission Blob

The gas kinematics based on the Hα emission line of LEDA 1678924 shows that LEDA 1678924 has a regularly rotating disk with a velocity field typical of disk galaxies. However, the velocity field shows a discontinuity at the location of MJ0818

+2257, which is unusual if we assume both galaxies are at the same redshift (for more detail, see the Appendix). In fact, the observed velocities clearly show a dual distribution. This suggests that MJ0818+2257 and LEDA 1678924 are kinematically decoupled, implying that they are two independent systems. As observed in Section 3.2, MJ0818+2257 and LEDA 1678924 are at different redshifts. Hence, we use their corresponding systematic velocities to derive their individual velocity fields as presented in Figure 4. Here the derived kinematics is corrected for the inclination angle (i) of galaxy, following the relation $V_{\rm rot} = V_{\rm los}^{\rm obs}/\mathrm{Sin}(i)$. The inclination angle for MJ0818+2257 is estimated using $i = \mathrm{Cos}^{-1}(b/a)$, where a and b represent the sizes of major and minor axes of outer ellipse, respectively. Since the stellar emission lines from MJ0818+2257 are too faint to detect using MaNGA IFU data, it is not possible to derive the stellar kinematics.

In Figure 4, it can be noticed that MJ0818+2257 shows a clear gas rotation, similar to the rotating dwarf galaxies studied in A. C. Seth et al. (2014). Also, the gas velocity dispersion
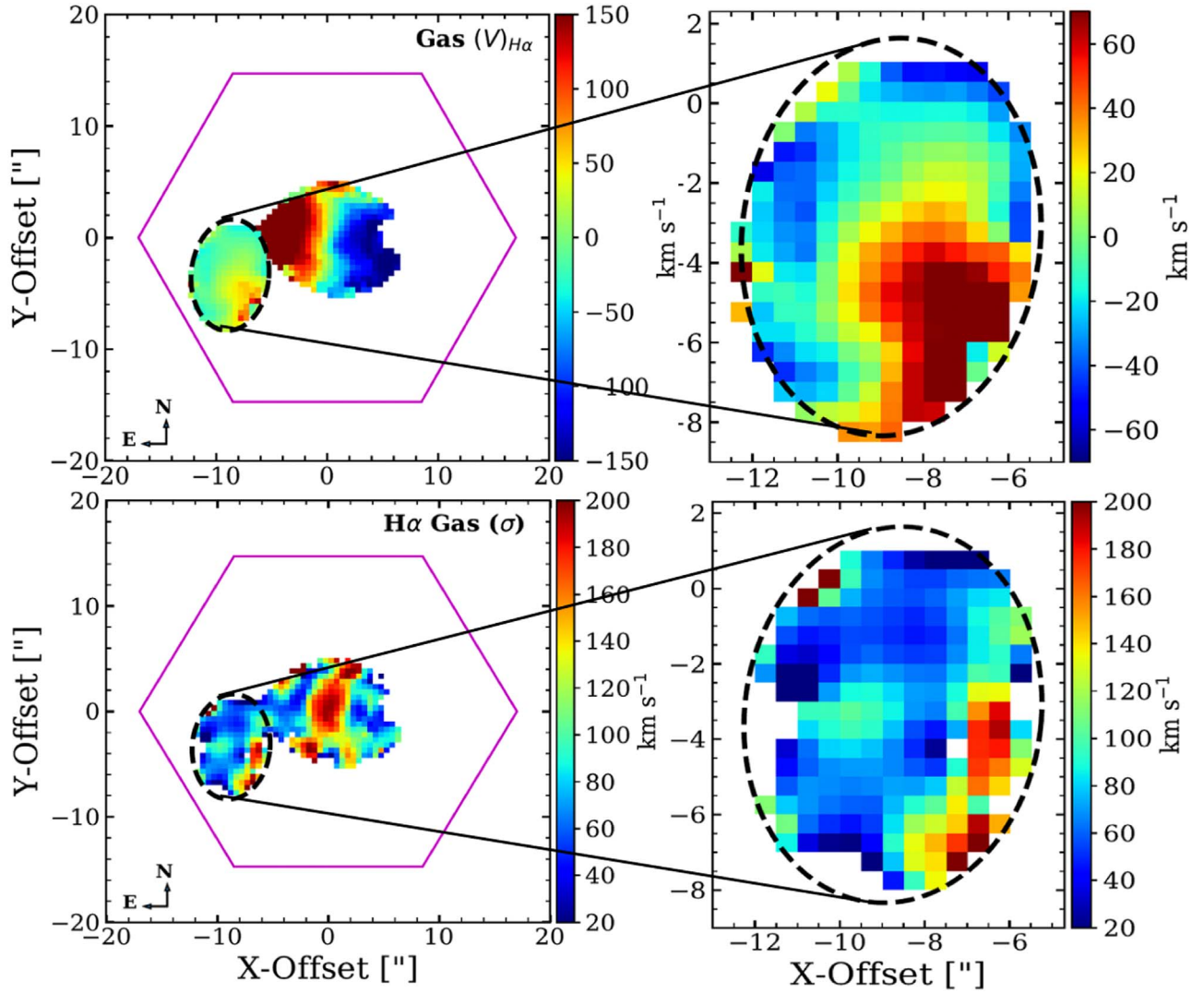
Figure 4. The rotation velocity of ionized gas derived using Hα emission line (top left panel). Top right panel represents its zoomed-in view centered on the central velocity of MJ0818+2257. Similarly, bottom left panel shows the velocity dispersion, and bottom right panel represents its zoomed-in view. In each panel, the location of MJ0818+2257 is marked by black dashed ellipse.

ranges over 50–100 km s^{-1}, which is again similar to typical rotating dwarf galaxies (e.g., A. C. Seth et al. 2014; A. Paswan et al. 2022). This finding safely rules out the possibility that MJ0818+2257 is an outlying emission blob originated due to the HsV process (see G. I. G. Józsa et al. 2009) or outflow ejections via AGN sources, which was previously reported by O. Bait et al. (2019). Overall, our results show that MJ0818 +2257 is an independent, rotating dwarf galaxy. Using the maximum gas rotation velocity (v), which is ~52 km s^{-1}, we estimate the dynamical mass ($M_{\rm dyn} \sim v^2 R/G$) of MJ0818 +2257 to be ~$5.3 \times 10^9 M_\odot$, within its disk radius (R) of ~8.5 kpc.

3.4. Views from Multifrequency Radio Continuum Emissions

In Figure 5, we show the optical r-band image overlaid with radio continuum contours (green) at 1.4, 3, 5, and 8.5 GHz. In each panel of Figure 5, white contours represent the [O III] $\lambda5007$ emission line from LEDA 1678924 and MJ0818+2257 observed in the MaNGA survey. Note that the [O III]$\lambda5007$ emission line is also observed from LEDA 1678982, but it is not possible here to show its extent in the form of contours due

to slit (3″ fiber) observations in the SDSS survey. Interestingly, it is noticeable that radio continuum emissions at different radio frequencies are seen from LEDA 1678982 only, while the three systems (i.e., MJ0818+2257, LEDA 1678924, and LEDA 1678982) are optically identified as hosting AGN sources (see BPT diagram). In fact, a radio jet–like structure from LEDA 1678982 can be observed in the 3 GHz radio band. However, there is a lack of close association between radio emission from LEDA 1678982 and MJ0818+2257, unlike the previous case of IC 2497, whose radio continuum emission was found closely associated with an HsV object (G. I. G. Józsa et al. 2009). Such a close association is essential for the origin of HsV objects because a plasma jet associated with AGN helps to clear a path through interstellar medium/intergalactic medium toward the nebulosity. Also, such a scenario is not even seen between LEDA 1678924 and MJ0818+2257. Thus, our result supports the fact that MJ0818+2257 is an independent dwarf galaxy.

4. Observed Nature of MJ0818+2257

Our analyses reveal the following: (i) the detection of the optical counterpart of MJ0818+2257, which reveals a well-
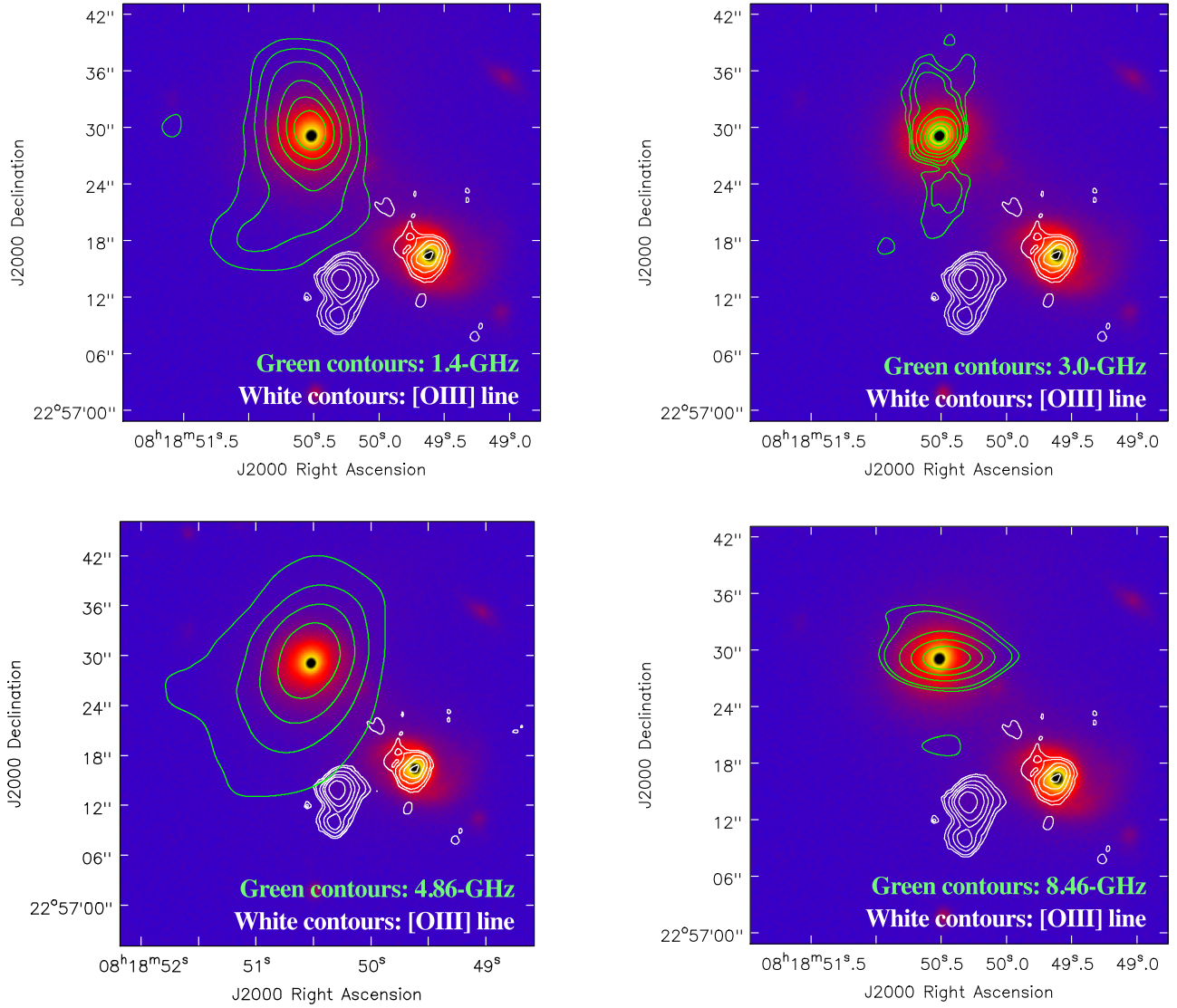
Figure 5. The radio continuum contours as shown by green solid lines at different frequencies that include 1.4 GHz (top left), 3 GHz (top right), 4.86 GHz (bottom left), and 8.46 GHz (bottom right) overlaid on optical g-band image from the DECaLS survey. In each panel, the white contours represent the MaNGA [O III]λ5007 emission line at the location of MJ0818+2257 and the spiral galaxy. Here north and east are up and left, respectively.

shaped dwarf galaxy-like morphology (see Figure 3) and is unlike the HsV object around IC 2497 (K. Schawinski et al. 2010); (ii) a rotating gaseous disk associated with MJ0818 +2257 (see Figure 4 which is similar to M60-UCD1; A. C. Seth et al. 2014). Both facts strongly indicate that MJ0818 +2257 is an independent low-luminosity dwarf galaxy that hosts a Seyfert-type AGN source (see BPT diagram in Figure 2). The galaxy has a diameter of $\sim$16.9 kpc. Its central surface brightness ($\mu_{0,r}$), estimated using the DeCALS r-band image, is found to be fainter than 23.8 mag arcsec^{-2} (see Appendix). The central surface brightness–based criteria used for classifying a galaxy into an LSB galaxy, given by C. Adami et al. (2006), indicates that MJ0818+2257 is an LSB dwarf galaxy. Such galaxies have low stellar surface densities and are metal poor but very gas rich (e.g., M. Honey et al. 2018). The blue color ($g - r < 0.8$) of MJ0818+2257 indeed confirms that it is metal poor, and the strong Hα and [O III]λ5007 emissions suggest that it is rich in ionized gas. The stellar mass, derived from the DeCALS r- and z-band images is $<3 \times 10^9 M_\odot$ (see Appendix).

Since MJ0818+2257 hosts an AGN, we derived its BH mass using the [O III]λ5007 bolometric nuclear luminosity of MJ0818+2257, assuming the Eddington ratio of a typical Seyfert type 2 class AGN (see Appendix). The mass of the BH hosted in MJ0818+2257 is found to be $\sim$6.5 $\times 10^6 M_\odot$, which falls in the SMBH category.

5. Discussion and Conclusion

In the literature, SMBHs are commonly found in massive galaxies that have a significant bulge component (N. J. McConnell & C.-P. Ma 2013). But recent discoveries show that massive BHs can be found in low-luminosity dwarf galaxies (A. E. Reines et al. 2013; V. F. Baldassare et al. 2015) and bulgeless disk galaxies as well (A. V. Filippenko & L. C. Ho 2003). For example, using optical SDSS spectroscopy, radio and X-ray data, studies by Reines et al. (e.g., A. E. Reines & A. T. Deller 2012; A. E. Reines et al. 2013, 2016, 2020) and others (J. E. Greene & L. C. Ho 2007; J. E. Greene 2012) reported more than a hundred dwarf galaxies that host BHs in the mass range of $10^5 \leqslant M_{\rm BH} \leqslant 10^6 M_\odot$. Recently, using

MaNGA IFU data, M. Mezcua & H. Domínguez Sánchez (2020) also reported a total of 37 AGN dwarf galaxies hosting IMBHs ($M_{BH} \sim 10^5 \, M_\odot$), which were previously missed with slit spectroscopy due to their off-nuclear AGN activities. Also, an SMBH ($>10^6 \, M_\odot$) was detected in the ultracompact dwarf galaxy M60-UCD1 using near infrared-IFU observations (A. C. Seth et al. 2014).

Considering these past studies, our discovery of an AGN and an SMBH ($\sim 10^6 \, M_\odot$) in the dwarf LSB galaxy MJ0818+2257 is important for several reasons. First, it shows the importance of using ionized emission lines for the detection of accreting massive BHs in low-luminosity sources such as MJ0818+2257. It also shows that IFU facilities such as MaNGA play a critical role for discovering rare low-luminosity galaxies that can be detected only from emission-line observations and not only optical imaging observations. For example, [O III] or Hα emission in combination with UV continuum imaging has been used to detect faint galaxies even in our nearby Universe (J. Yadav et al. 2022). Second, SMBHs in dwarfs are important for establishing the scaling relations between the mass of BHs and their host galaxies at the lowest mass scales (e.g., J. Kormendy & L. C. Ho 2013; M. C. Bentz & E. Manne-Nicholas 2018; Z. Schutte et al. 2019). The third reason is that it raises the possibility of detecting large populations of SMBHs in dwarf LSB galaxies at high redshifts using IFU facilities such as the JWST. This is especially important because large populations of such dwarf galaxies are expected to exist at early epochs and may be important for reionization of the Universe (H. Atek et al. 2024). MJ0818+2257 is thus a good example of the low-redshift counterpart of such dwarf galaxies.

Another important fact is that the SMBH in MJ0818+2257 may represent a seed BH from early epochs in the Universe. This is because the host galaxy is an LSB dwarf, and such galaxies do not show signatures of a rich merger history that would have led to the growth of their nuclear BH. LSB galaxies are known to have low stellar surface densities, low metallicities, and low star formation rates. For example, giant LSB galaxies that also have diffuse stellar disks and have not undergone many mergers have relatively low-mass SMBHs (10^5–$10^7 \, M_\odot$) that lie below the $M-\sigma$ relation for low-z galaxies (S. Subramanian et al. 2016). There are also cosmological models and simulations of BH evolution that suggest that low-mass dwarf galaxies are potential systems hosting pristine BHs that are the seeds for SMBHs in more massive galaxies (D. Angles-Alcazar et al. 2017; M. Habouzit et al. 2017). The SMBH-mass-to-stellar-mass ratio in MJ0818+2257 i.e., $M(BH)/M(^*) > 0.022$, is slightly higher than the local value of ~ 0.001 (see Appendix A; P. Dayal 2024). Thus, the SMBH in MJ0818+2257 may represent a massive seed BHs from early epochs that has remained relatively pristine due to a lack of mergers in its evolutionary history.

There are mainly three processes that lead to the formation of massive seed BHs at early epochs. They include the direct cloud collapse models that form heavy seed BHs, the evolution of $\sim 100 \, M_\odot$ Population III stars into SMBHs via galaxy mergers, and the evolution of dense stellar clusters at early epochs (V. Cammelli et al. 2024). But since MJ0818+2257 is a bulgeless, metal-poor dwarf, the origin of its SMBH can best be explained only via the direct collapse of a pristine gas cloud, which is similar to the recently discovered X-ray quasar, UHZ1, at $z \sim 10$, that has been confirmed to harbor a heavy seed BH using JWST/NIRCam observations (Á. Bogdán et al.

2024). Thus, dwarfs such as MJ0818+2257 are ideal low-z laboratories for placing constraints on the nature and mass of seed BHs, as well as for providing inputs for modeling their growth.

Appendix A
Optical Photometry and Stellar Mass Estimation

The optical counterpart of MJ0818+2257 is best detected in the DeCALS g-band image (see Figure 3) but is also faintly detected in the r-, i-, and z-band images (see Figure 6). Furthermore, Figure 7 justifies that the emission in most of these bands is mainly dominated by stellar continuum emission and is not due to strong nebular emission lines. However, some faint light contamination due to LEDA 1678924 cannot be ignored in these broadband filters.

The optical detection of MJ0818+2257 over multiple bands offers an opportunity to constrain its stellar mass. There are several methods to estimate the stellar mass of a galaxy, and most of these methods involve the stellar population's mass-to-light ratio (M/L). Although the M/L obtained by fitting the stellar population synthesis models to the spectral energy distribution (SED; J. Walcher et al. 2011; C. Conroy 2013; S. Courteau et al. 2014) of a galaxy is the most reliable one, in the absence of a broad span of an SED, the color-based M/L estimates are widely used to establish several calibrations that provide the stellar mass of a galaxy (e.g., E. F. Bell & R. S. de Jong 2001; E. F. Bell et al. 2003; A. Gallazzi & E. F. Bell 2009; S. S. McGaugh & J. M. Schombert 2014). These calibrations are made after taking into account the underlying stellar population, dust attenuation, and chemical evolution. Note that color-based stellar mass (or M/L) does not deviate much from that of the SED-based estimates (J. C. Roediger & S. Courteau 2015). Using a mock galaxy sample, J. C. Roediger & S. Courteau (2015) have demonstrated that the stellar masses derived based on optical color and SED fitting are consistent within a scatter of 0.2 dex and yield similar results when these methods are applied to galaxies having their stellar masses in the range of $\sim 10^8$–$10^{11}\,M_\odot$.

Since MJ0818+2257 is detected in the DeCALS g, r, i, and z bands only, this is not enough to construct the SED, and we use the color-based approach to estimate the M/L by following the calibration given below (E. F. Bell et al. 2003):

$$\mathrm{Log(M/L)} = a_\lambda + (b_\lambda \times \mathrm{color}), \tag{A1}$$

where M/L is in solar units and a_λ and b_λ are color-based coefficients (E. F. Bell et al. 2003). The stellar mass of MJ0818+2257 is estimated using the z-band luminosity and $(r - z)$ color by following the above calibration. For this combination of luminosity and color, the values of a_λ and b_λ are -0.041 and 0.463 (E. F. Bell et al. 2003). It is to be noted that the above calibration yields a wavelength-dependent error in the range of ~ 0.1–0.3 dex for the optical bands. However, this error is observed to be minimal when we use the redder band luminosity because it is less sensitive to extinction and the age of the stellar population compared to bluer bands (C. A. Tremonti et al. 2004). We therefore choose z-band luminosity, which is also less contaminated by strong nebular emission lines. The z-band luminosity is derived using the relation, $L = 10^{0.4 \times (4.50 - M_z)}\,L_\odot$, where M_z represents the absolute magnitude of the source in z-band and is estimated using the relation $M_z = m_z - 5\mathrm{Log}(D_L - 1) - A_\lambda$, where m_z and D_L are the apparent magnitude in z band and the luminosity distance of the source, respectively, and A_λ represents the dust extinction correction. In the latter relation, we take the value of A_λ as zero because the observed flux ratio $f_{\mathrm{H}\alpha}/f_{\mathrm{H}\beta}$ (i.e.,Balmer decrement) at the location of MJ0818+2257, derived using the MaNGA IFU data, is found to be less than the expected theoretical value of 2.86. Such low values are often associated with extremely low reddening, as has also been noticed in several past studies (S. Ramya et al. 2009; M. L. P. Gunawardhana et al. 2013; A. Paswan et al. 2018).

In order to calculate the stellar mass of MJ0818+2257, we first estimated its apparent magnitude (m_z) derived via
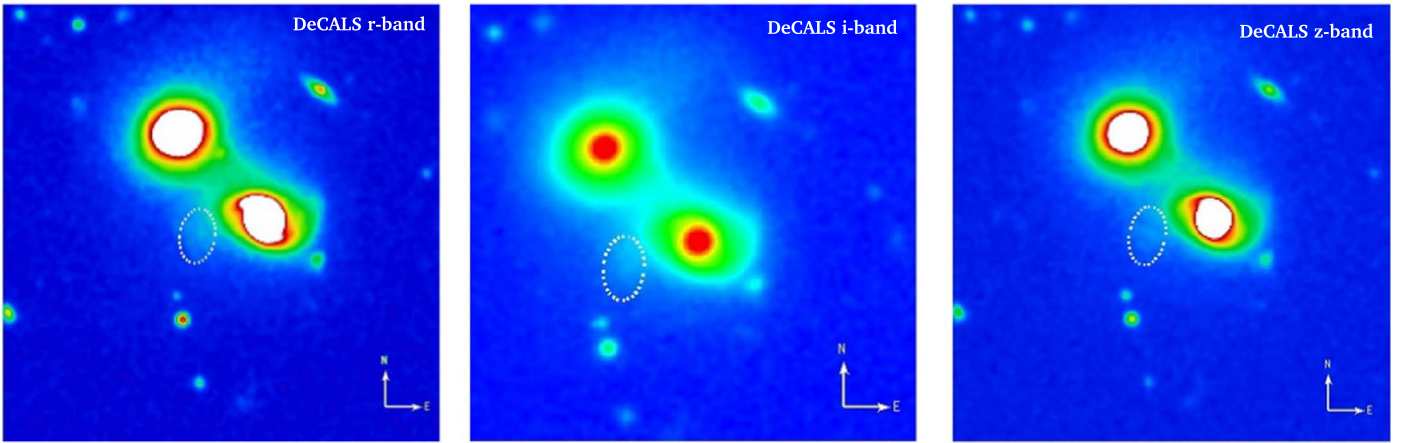
Figure 6. Deep optical *r*- (left), *i*- (middle), and *z*-band (right) images of LEDA 1678924 and LEDA 1678982, taken from the DeCALS survey. In each panel, a dotted ellipse represents the location of MJ0818+2257.
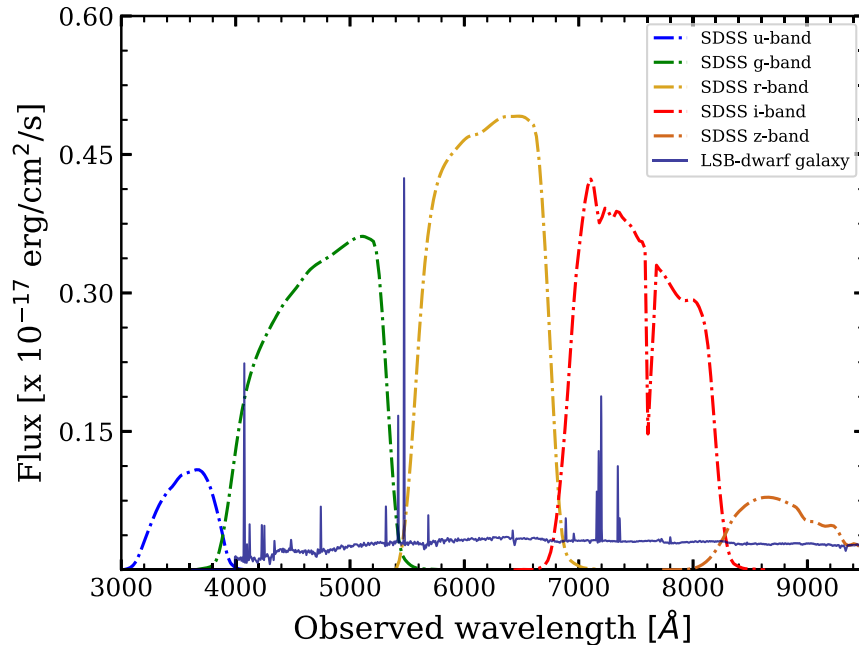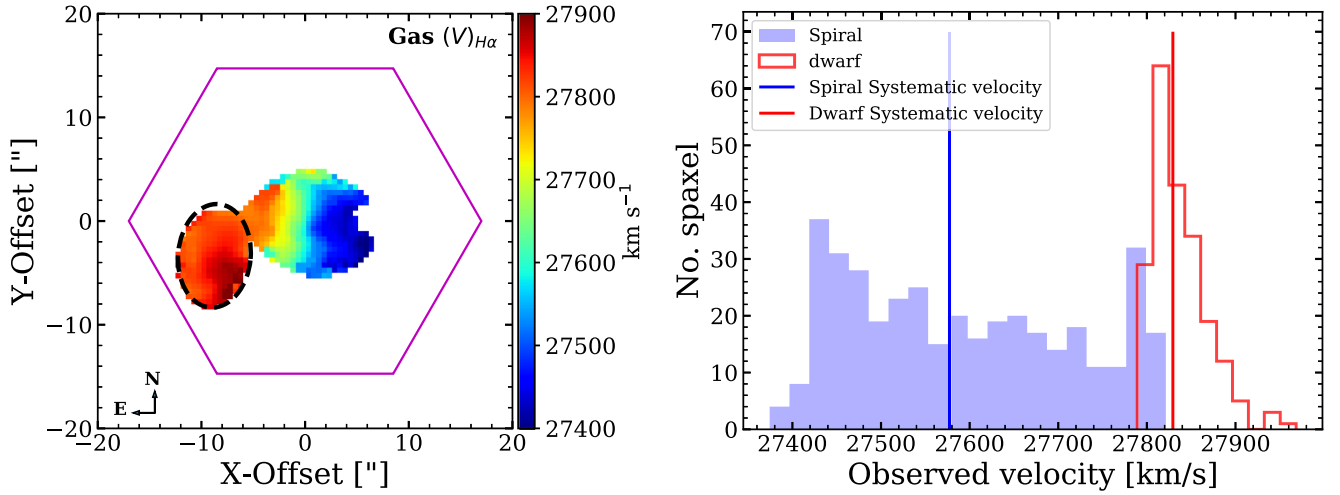

Figure 7. The observed spectrum at the center of the outlying emission blob (i.e., MJ0818+2257) overlaid with the five SDSS filter bands, showing contaminations of emission-line features with the filter bands.

photometry within the aperture ($3{.}{''}1 \times 4{.}{''}9$) as shown in Figure 3(a). The value of m_z is found as $\sim$18.80. Similarly, the apparent magnitudes of MJ0818+2257 in the DeCALS *g*- and *r*-band images is estimated to be $\sim$20.24 and $\sim$19.44, respectively. Consequently, the values of $(g - r)$ and $(r - z)$ are found to be $\sim$0.8 and $\sim$0.64, respectively. Using these estimates of magnitudes and colors and following the relations described earlier, we find the stellar mass of MJ0818+2257 as $\sim$$3 \times 10^9\,M_\odot$. While the magnitudes of MJ0818+2257 are derived within the aperture $3{.}{''}1 \times 4{.}{''}9$, we derive its central surface brightness ($\mu_{0,r} \sim 23.8$ mag arcsec^{-2}) using the aperture of $1''$ located at the center. This aperture is particularly selected as $1''$ because it is comparable to the point-spread function of DeCALS images. It is important to note here that the derived values of magnitudes, colors, stellar mass, and central surface brightness must be taken as their upper limits because diffuse light contamination within the selected apertures due to LEDA 1678924 (i.e., a galaxy in the projected vicinity of MJ0818+2257) is not removed.

Appendix B
Observed Decoupled Gas Kinematics

Using Hα emission line, in the left panel of Figure 8, we present the observed line-of-sight velocity (V_{los}) map for both LEDA 1678924 and the outlying emission blob (marked with a dashed ellipse). In this figure, it can be noticed that the observed V_{los} corresponding to the extent of LEDA 1678924 ranges over $\sim$27,400–27,800 km s^{-1}, having a smooth gradient from its outer west side to east side, with a median value of $\sim$27,580 km s^{-1} at its central region. And, it is $\sim$27,790–27,920 km s^{-1} over the outlying emission blob, with a median value of $\sim$27,855 km s^{-1} at its central region. The velocity histogram is also shown in the right panel of Figure 8. The observed V_{los} of the outlying emission blob indicates a discontinuity against a regular V_{los} of LEDA 1678924 (i.e., a spiral rotating disk galaxy). In the right panel of Figure 8, one can see clearly two different V_{los} distributions whose central velocities significantly differ from each other. Such a

Figure 8. Left: the observed velocity map for LEDA 1678924 (i.e., spiral galaxy) and LSB dwarf galaxy (i.e., outlying emission blob). Right: their corresponding histogram velocity distributions and their respective systematic velocities are shown by vertical lines.

discontinuity in the velocities of the two objects can only be seen if they are kinematically decoupled or external to each other. This also implies that both the objects have their own different systematic velocities as shown by the two vertical lines in the right panel of Figure 8. Thus, LEDA 1678924 and the outlying emission blob can be treated as two separate systems.

Appendix C
BH Mass Estimation

There are several methods to calculate the BH mass in a galaxy (e.g., A. Marconi & L. K. Hunt 2003; J. Kormendy & L. C. Ho 2013; N. J. McConnell & C.-P. Ma 2013), among which is a method that uses the width of the broad component of the Hα emission line, which is widely used in the literature (e.g., J. E. Greene & L. C. Ho 2007; S. Ramya et al. 2011). Since we do not observe the Hα broad component in the case of our bulgeless LSB dwarf galaxy, MJ0818+2257, we choose an alternate method that estimates the BH mass. We derive the BH mass of MJ0818+2257 using its Eddington luminosity (L_{Edd}) $\simeq 1.3 \times 10^{38}$ ($M_{\mathrm{BH}}/M_{\odot}$), representing an upper limit to the luminosity produced by a BH having mass M_{BH}. This limit decides the balance between the outward radiation pressure from the accreting matter and the inward gravitational pressure exerted by the BH. Here, the accreting mass rate can be parameterized by Eddington ratio ($l_{\mathrm{Edd}} = L_{\mathrm{Bol}}/L_{\mathrm{Edd}}$), which is the ratio of the bolometric luminosity (L_{Bol}) to the Eddington luminosity (L_{Edd}) for a given BH mass (M_{BH}). The Eddington ratio can be given as (J.-M. Wang & E.-P. Zhang 2007)

$$l_{\mathrm{Edd}} = 0.1(L_{\mathrm{Bol}}/1.4 \times 10^{44} \, \mathrm{erg \, s}^{-1})(M_{\mathrm{BH}}/M_{\odot}). \quad (C1)$$

We observationally constrain the bolometric luminosity using the [O III]λ5007 line luminosity observed in the MaNGA emission line map and the relation $L_{\mathrm{Bol}}/L_{\mathrm{[OIII]}\lambda5007} \simeq 3500$ (T. M. Heckman et al. 2004). Since MJ0818+2257 falls in the category of Seyfert type 2 class as observationally constrained by our BPT diagnostic (see Figure 2), we therefore assume its Eddington ratio (l_{Edd}) spanned over $\sim 1.9 \times 10^{-3}$ to $\sim 6.2 \times 10^{-1}$ with the median value $\sim 4.2 \times 10^{-2}$ (V. Singh et al. 2011). With this assumption and using Equation (C1) and the median value of l_{Edd}, we reach the BH mass hosted by MJ0818+2257 as $\sim 6.5 \times 10^{6} \, M_{\odot}$. Assuming an upper limit of

the galaxy stellar mass to be $M^{(*)} < 3 \times 10^{9} \, M_{\odot}$ (see Appendix A), the SMBH-mass-to-stellar-mass ratio is $M(\mathrm{BH})/M^{(*)} > 0.022$. This is slightly higher than the local value of ~ 0.001.

ORCID iDs

Abhishek Paswan (ID) https://orcid.org/0000-0002-2657-9044
Mousumi Das (ID) https://orcid.org/0000-0001-8996-6474
K Rubinur (ID) https://orcid.org/0000-0001-5574-5104

References

Adami, C., Scheidegger, R., Ulmer, M., et al. 2006, A&A, 459, 679
Angles-Alcazar, D., Faucher-Giguere, C.-A., Quataert, E., et al. 2017, MNRAS, 472, L109
Atek, H., Labbé, I., Furtak, L. J., et al. 2024, Natur, 626, 975
Bait, O., Wadadekar, Y., & Barway, S. 2019, MNRAS, 485, 428
Baldassare, V. F., Reines, A. E., Gallo, E., & Greene, J. E. 2015, ApJL, 809, L14
Baldwin, J. A., Phillips, M. M., & Terlevich, R. 1981, PASP, 93, 5
Becker, R. H., White, R. L., & Helfand, D. J. 1995, ApJ, 450, 559
Bell, E. F., & de Jong, R. S. 2001, ApJ, 550, 212
Bell, E. F., McIntosh, D. H., Katz, N., & Weinberg, M. D. 2003, ApJS, 149, 289
Bellovary, J., Volonteri, M., Governato, F., et al. 2011, ApJ, 742, 13
Bentz, M. C., & Manne-Nicholas, E. 2018, ApJ, 864, 146
Bogdán, Á., Goulding, A. D., Natarajan, P., et al. 2024, NatAs, 8, 126
Bundy, K., Bershady, M. A., Law, D. R., et al. 2015, ApJ, 798, 7
Cammelli, V., Monaco, P., Tan, J. C., et al. 2024, arXiv:2407.09949
Cappellari, M., & Emsellem, E. 2004, PASP, 116, 138
Cid Fernandes, R., Stasinska, G., Schlickmann, M. S., et al. 2010, MNRAS, 403, 1036
Conroy, C. 2013, ARA&A, 51, 393
Courteau, S., Cappellari, M., de Jong, R. S., et al. 2014, RvMP, 86, 47
Dayal, P. 2024, arXiv:2407.07162
Drory, N., MacDonald, N., Bershady, M. A., et al. 2015, AJ, 149, 77
Ferrarese, L., & Merritt, D. 2000, ApJL, 539, L9
Filippenko, A. V., & Ho, L. C. 2003, ApJL, 588, L13
Gallazzi, A., & Bell, E. F. 2009, ApJS, 185, 253
Gebhardt, K., Bender, R., Bower, G., et al. 2000, ApJL, 539, L13
Greene, J. E. 2012, NatCo, 3, 1304
Greene, J. E., & Ho, L. C. 2007, ApJ, 670, 92
Gunawardhana, M. L. P., Hopkins, A. M., Bland-Hawthorn, J., et al. 2013, MNRAS, 433, 2764
Habouzit, M., Volonteri, M., & Dubois, Y. 2017, MNRAS, 468, 3935
Heckman, T. M., Kauffmann, G., Brinchmann, J., et al. 2004, ApJ, 613, 109
Honey, M., van Driel, W., Das, M., & Martin, J.-M. 2018, MNRAS, 476, 4488
Józsa, G. I. G., Garrett, M. A., Oosterloo, T. A., et al. 2009, A&A, 500, L33
Kormendy, J., & Ho, L. C. 2013, ARA&A, 51, 511

Lacerda, E. A. D., Cid Fernandes, R., Couto, G. S., et al. 2018, MNRAS, 474, 3727

Lacy, M., Baum, S. A., Chandler, C. J., et al. 2020, PASP, 132, 035001

Law, D. R., Cherinka, B., Yan, R., et al. 2016, AJ, 152, 83

Marconi, A., & Hunt, L. K. 2003, ApJL, 589, L21

McConnell, N. J., & Ma, C.-P. 2013, ApJ, 764, 184

McGaugh, S. S., & Schombert, J. M. 2014, AJ, 148, 77

Mezcua, M., & Domínguez Sánchez, H. 2020, ApJL, 898, L30

O'Donnell, J. E. 1994, ApJ, 422, 158

Oke, J. B. 1974, ApJS, 27, 21

Pacucci, F., Nguyen, B., Carniani, S., Maiolino, R., & Fan, X. 2023, ApJL, 957, L3

Paswan, A., Omar, A., & Jaiswal, S. 2018, MNRAS, 473, 4566

Paswan, A., Saha, K., Borgohain, A., Leitherer, C., & Dhiwar, S. 2022, ApJ, 929, 50

Ramya, S., Prabhu, T. P., & Das, M. 2011, MNRAS, 418, 789

Ramya, S., Sahu, D. K., & Prabhu, T. P. 2009, MNRAS, 396, 97

Reines, A. E., Condon, J. J., Darling, J., & Greene, J. E. 2020, ApJ, 888, 36

Reines, A. E., & Deller, A. T. 2012, ApJL, 750, L24

Reines, A. E., Greene, J. E., & Geha, M. 2013, ApJ, 775, 116

Reines, A. E., Reynolds, M. T., Miller, J. M., et al. 2016, ApJL, 830, L35

Reines, A. E., Sivakoff, G. R., Johnson, K. E., & Brogan, C. L. 2011, Natur, 470, 66

Roediger, J. C., & Courteau, S. 2015, MNRAS, 452, 3209

Schawinski, K., Evans, D. A., Virani, S., et al. 2010, ApJL, 724, L30

Schutte, Z., Reines, A. E., & Greene, J. E. 2019, ApJ, 887, 245

Seth, A. C., van den Bosch, R., Mieske, S., et al. 2014, Natur, 513, 398

Singh, V., Shastri, P., & Risaliti, G. 2011, A&A, 533, A128

Subramanian, S., Ramya, S., Das, M., et al. 2016, MNRAS, 455, 3148

Tremonti, C. A., Heckman, T. M., Kauffmann, G., et al. 2004, ApJ, 613, 898

Volonteri, M. 2010, A&ARv, 18, 279

Walcher, J., Groves, B., Budavári, T., & Dale, D. 2011, Ap&SS, 331, 1

Wang, J.-M., & Zhang, E.-P. 2007, ApJ, 660, 1072

Westfall, K. B., Cappellari, M., Bershady, M. A., et al. 2019, AJ, 158, 231

Yadav, J., Das, M., Barway, S., & Combes, F. 2022, A&A, 657, L10

Zhang, K., Yan, R., Bundy, K., et al. 2017, MNRAS, 466, 3217